Magneto-optical transport properties of monolayer WSe_2

M. Tahir* and P. Vasilopoulos†
Department of Physics, Concordia University, Montreal, Quebec, Canada H3G 1M8
(Received 11 May 2016; published 11 July 2016)

The recent experimental realization of a high quality WSe_2 leads to the possibility of magneto-optical measurements and the manipulation of the spin and valley degrees of freedom. We study the influence of the very strong spin-orbit coupling and of the anisotropic lifting of the valley pseudospin degeneracy on its magnetotransport properties. The energy spectrum of WSe_2 is derived and discussed in the presence of a perpendicular magnetic field B. Correspondingly we evaluate the magneto-optical Hall conductivity and the optical longitudinal conductivity as functions of the frequency, magnetic field, and Fermi energy. They are strongly influenced by the field B and the strong spin splitting. The former exhibits valley polarization and the latter beatings of oscillations. The magneto-optical responses can be tuned in two different regimes: the microwave-to-terahertz regime and the visible-frequency one. The absorption peaks involving the $n = 0$ LL appear in between these two regimes and show a magnetic control of the spin and valley splittings. We also evaluate the power absorption spectrum.

DOI: 10.1103/PhysRevB.94.045415

I. INTRODUCTION

Graphene possesses extraordinary properties but its application to device fabrication is limited by its zero band gap which makes graphene transistors suffer from a low on-off current ratio [1]. This has led to intensive investigation of alternative materials with a finite band gap including silicene [2], germanene [3], and the group VI transition-metal dichalcogenides MX_2, $M = \mathrm{Mo,W}$; $X = \mathrm{S,Se}$ [4–8]. This MX_2 family is an intriguing class of semiconductors when thinned down to monolayers. The valence and conduction band extrema are located at both K and K' points at the corners of the hexagonal Brillouin zone. The K and K' points are related to each other by time-reversal symmetry and give rise to the valley degree of freedom of the band-edge electrons and holes [9–12]. It has been demonstrated that a monolayer of MoS_2 has reasonable in-plane carrier mobility, high thermal stability, and good compatibility with standard semiconductor manufacturing [5]. These properties render monolayer MoS_2 a promising candidate for a wide range of applications, including photoluminescence at visible wavelengths [9,13], photodetectors with high responsivity [11], and field-effect transistors [5,14,15].

Compared to MoS_2 the material WSe_2 has a much stronger spin-orbit-coupling (SOC): in the valence band it is $2\lambda_v' = 450$ meV and in the conduction band $2\lambda_c' = 30$ meV. This and its high quality provide an excellent system for spin and valley control [16,17]. A high-mobility WSe_2 transistor has been demonstrated at room temperature [18]. Although WSe_2 is a direct-band-gap semiconductor ($2\Delta = 1.7$ eV), the lifting of the valley degeneracy allows for optical manipulation of the electron valley index. This has been realized by applying a magnetic field normal to the two-dimensional (2D) layer; see Refs. [16,17] which clearly demonstrate the lifting of the valley degeneracy in WSe_2. This is achieved by monitoring the energy splitting between the two circularly polarized luminescence components, σ^+ and σ^-, associated with optical recombination in the two valleys.

References [16,17] studied optical transitions in a monolayer of WSe_2 and related compounds in magnetic fields. Direct optical transitions in a WSe_2 monolayer occur at the edge of the Brillouin zone, which mainly consists of strongly localized d orbitals of the transition metal. This is in contrast with GaAs and other conventional semiconductors used in optoelectronics in which the direct optical band gap is situated at the center of the Brillouin zone. In a WSe_2 monolayer there are several possible contributions to the Zeeman splitting as the emission of circularly polarized light originates from states with contrasting valley index, spin, and orbital magnetic moment. As the valleys can be selectively addressed, these experiments allow the different contributions to the Zeeman splitting to be determined. A magneto-optical investigation in high-quality samples of WSe_2 appeared in Ref. [19].

Optical transport properties have been evaluated for graphene and a good agreement exists between theory and experiment [20]. Magneto-optical properties of topological insulators (TIs) [21] and other single-layer materials, such as MoS_2 [22] and silicene [23], have also been investigated. Several properties of WSe_2 have been studied at zero magnetic field [16,17]. In a finite magnetic field though Landau levels (LLs) are formed and transitions between them generate specific absorption lines in the magneto-optical conductivity. We are aware though only of the experimental work [19] but of no theoretical one on the magnetotransport properties of WSe_2. Accordingly, studying these properties is timely and expected to increase our understanding of this material. Further, WSe_2 is expected to show strong spin- and valley-controlled properties [16,17] in contrast to graphene. As will be shown, an important difference with it and other 2D systems, in which the magneto-optical response occurs in the terahertz (THz) regime, is that in WSe_2 it can be tuned to the microwave-to-THz and visible-frequency ranges. This is similar to phosphorene's response [24].

In this work we study the ac magnetotransport properties of a WSe_2 monolayer in a perpendicular magnetic field B. Using the spectrum of this material and general, Kubo-type formulas,

*m.tahir06@alumni.imperial.ac.uk
†p.vasilopoulos@concordia.ca

expressed explicitly in terms of single-particle eigenstates and eigenvalues, we evaluate the Hall and longitudinal conductivities as well as the absorption spectrum. In Sec. II we present the basics of the model, in Sec. III the conductivity expressions and limited theoretical calculations, and in Sec. III numerical results. We summarize in Sec. V.

II. MODEL

We consider a monolayer of WSe_2 in the (x,y) plane in the presence of intrinsic SOC, spin and valley Zeeman fields, and a normal magnetic field B. Extending the 2D, Dirac-type Hamiltonian of WSe_2 for $B=0$ [25], we have

$$H^{s\eta} = v_F(\eta\sigma_x\Pi_x + \sigma_y\Pi_y) + \Delta\sigma_z + \eta s(\lambda_c\sigma_+ + \lambda_v\sigma_-) + sM_z - \eta M_v. \quad (1)$$

Here $\eta=\pm1$ for valleys K and K', Δ is the mass term that breaks the inversion symmetry, $\lambda_c=\lambda_{c'}/2$, $\lambda_v=\lambda'_v/2$, $(\sigma_x,\ \sigma_y,\ \sigma_z)$ are the Pauli matrices for the valence and conduction bands, $\sigma_\pm=\sigma_0\pm\sigma_z$, v_F $(5\times10^5$ m/s) is the Fermi velocity, and $s_z=+1(-1)$ is the up (down) spin. Further, $M_z=g'\mu_B B/2$ is the Zeeman exchange field induced by ferromagnetic order, g' the Landé g factor ($g'=g'_e+g'_s$), and μ_B the Bohr magneton [16,17]. Also, $g'_e=2$ is the free-electron g factor and $g'_s=0.21$ is the out-of-plane factor due to the strong SOC. The last term, $M_v=g'_v\mu_B B/2$, breaks the valley symmetry of the levels and $g'_v=4$ [16,17]. Further, $\Pi=\mathbf{p}+e\mathbf{A}$ is the 2D canonical momentum with vector potential $\mathbf{A}$. Using the Landau gauge with $\mathbf{A}=(0,Bx,0)$ and diagonalizing the Hamiltonian (1) gives the eigenvalues

$$E_n^{s\eta,\gamma} = s\eta(\lambda_c+\lambda_v) + sM_z - \eta M_v + \gamma E_n^{s\eta}, \quad (2)$$

where $E_n^{s\eta}=[n\hbar^2\omega_c^2+\Delta_{s\eta}^2]^{1/2}$, $\omega_c=(2eB/\hbar)^{1/2}$ is the cyclotron frequency, $\gamma=\pm1$ represents electron and hole states, respectively, and $\Delta_{s\eta}=\Delta+s\eta(\lambda_c-\lambda_v)$. The eigenvalues (2) become simpler upon noticing the inequality $\hbar\omega_c\ll\Delta_{s\eta}$. Expanding the square root in $E_n^{s\eta}$ gives

$$E_n^{s\eta,\gamma} \approx s\eta(\lambda_c+\lambda_v)+sM_z-\eta M_v+\gamma\Delta_{s\eta}+\gamma n\frac{\hbar^2\omega_c^2}{2\Delta_{s\eta}}. \quad (3)$$

This is a usual, linear in n and B LL spectrum. Using $\Delta_{s\eta}\gg\eta s\lambda$ the last term is equal $\gamma n(\hbar^2\omega_c^2/2\Delta)(1+\eta\lambda)$. This gives a spin splitting $E(s=1)-E(s=-1)=2M_z+n\eta\lambda(\hbar^2\omega_c^2/\Delta)$ in the conduction band and $2\eta\lambda-n\eta\lambda(\hbar^2\omega_c^2/\Delta)$ in the valence band. The term $n(\hbar^2\omega_c^2/2\Delta)\propto nB$ is about twice as big as M_z and much smaller than λ. It's important in the conduction band but negligible in the valence band in which $\lambda\approx450$ meV. For very weak fields B the linear dispersion, due to the huge band gap, has been discussed in Refs. [4–8,25].

The eigenfunctions corresponding to Eq. (2) are obtained as

$$\Psi_n^{s\eta,\gamma} = \frac{e^{ik_y y}}{\sqrt{L_y}}\begin{pmatrix}\eta C_n^{s\eta,\gamma}\phi_n\\ D_n^{s\eta,\gamma}\phi_{n-1}\end{pmatrix}, \quad (4)$$

where $C_n^{s\eta,\gamma}=\sqrt{n}\hbar\omega_c/[n\hbar^2\omega_c^2+(\Delta_{s\eta}-\gamma E_n^{s\eta})^2]^{1/2}$ and $D_n^{s\eta,\gamma}=(-\Delta_{s\eta}+\gamma E_n^{s\eta})/[n\hbar^2\omega_c^2+(\Delta_{s\eta}-\gamma E_n^{s\eta})^2]^{1/2}$; $\phi_n(x)$ are harmonic oscillator functions. The eigenvalues for $n=0$ are

$$E_0^{s,+} = \Delta+2s\lambda_c+sM_z-M_v,$$
$$E_0^{s,-} = -\Delta-2s\lambda_v+sM_z+M_v \quad (5)$$

and the corresponding eigenfunctions

$$\Psi_0^{s,+}=\frac{e^{ik_y y}}{\sqrt{L_y}}\begin{pmatrix}\phi_0\\0\end{pmatrix},\quad \Psi_0^{s,-}=\frac{e^{ik_y y}}{\sqrt{L_y}}\begin{pmatrix}0\\\phi_0\end{pmatrix}. \quad (6)$$

To better appreciate the spectrum (2) one can contrast it with that for $B=0$ given by

$$E_p^{s,\eta}=s\eta(\lambda_c+\lambda_v)+sM_z-\eta M_v+\gamma\left[v^2\hbar^2k^2+\Delta_{s\eta}^2\right]^{1/2}. \quad (7)$$

Here $\gamma=1(-1)$ denotes the conduction (valence) band, $s=1(-1)$ is for spin up (down), and $\eta=1(-1)$ for the $K(K')$ valley. Further, k is the 2D wave vector. The spectrum (7) is shown in Fig. 1 versus ka where $a=0.331$ nm is the lattice constant.

We present the eigenvalues given by Eq. (2), as functions of the field B, in Fig. 2. The top and panel is for the conduction band and the bottom ones for the valence band with finite spin M_z and valley M_v Zeeman fields. We find the following. (i) In contrast to the $\sqrt{B}$ dependence in graphene or silicene, the LLs grow linearly with B. This is obvious from Eq. (3) which holds well because $\hbar\omega_c\ll\Delta_{\eta s}$. (ii) For $M_z=M_v=0$ the spin splitting in the conduction band is enhanced due to the last term in Eq. (3). It is approximately an order of magnitude

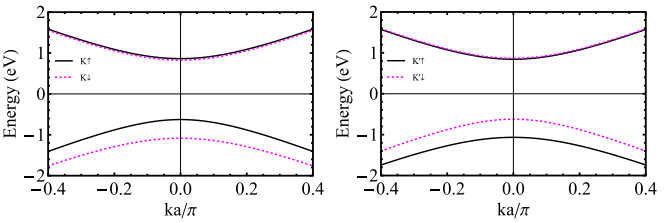

FIG. 1. Band structure of WSe_2 in the absence of a magnetic field B. The left panel is for the K valley and the right one for the K' valley.

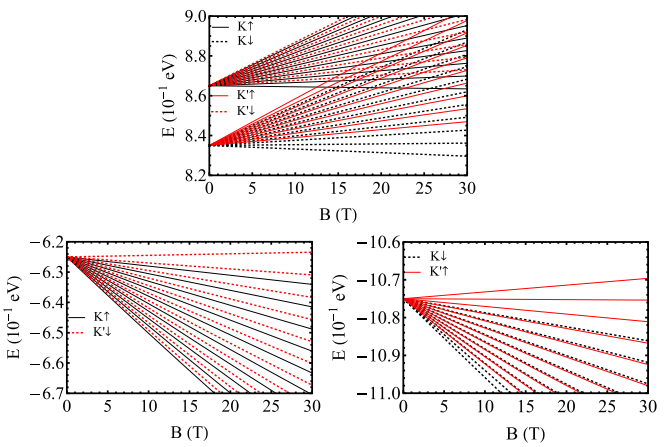

FIG. 2. Band structure of MoS_2 versus magnetic field B including spin and valley Zeeman fields. The top panel is for the conduction band and the bottom ones for the valence band.

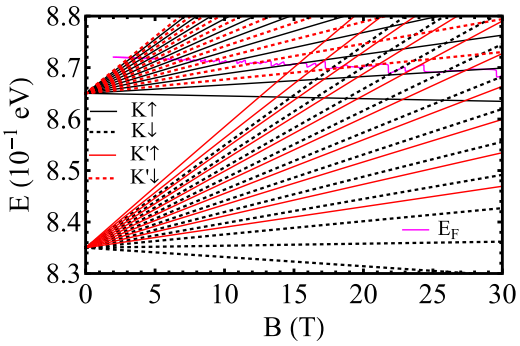

FIG. 3. Fermi level of WSe_2 as a function of the magnetic field B for $T = 1$ K.

larger than M_z term and depends linearly on the LL index n and field B: for $n = 5$ it is 33.3 meV at $B = 30$ T. (iii) As Fig. 2 shows, the energies of the spin-up (-down) LLs at the K valley are different than those of the spin-down (-up) at the K' valley. This is in contrast to MoS_2 where the spin splitting is negligible in the conduction band [6]. On the other hand, in the valence band the spin splitting is 450 meV and is the same as that for $B = 0$. (vi) The $n = 0$ LL is valley degenerate for $M_z = M_v = 0$ in both the conduction and valence bands.

The density of states (DOS) is given by

$$D(E) = \frac{1}{S_0} \sum_{n,\eta,s,k_y} \delta\left(E - E_n^{s\eta,\gamma}\right), \tag{8}$$

where $S_0 = L_x L_y$ is area of the system. The sum over k_y can be evaluated using the prescription $(k_0 = L_x/2l^2) \sum_{k_y} \to (L_y/2\pi) g_s g_v \int_{-k_0}^{k_0} dk_y = (S_0/D_0) g_s g_v$, $D_0 = 2\pi l^2$; g_s and g_v are the spin and valley degeneracy factors. We use $g_s = g_v = 1$ in the present work due to the lifting of the spin and valley degeneracies. The Fermi level E_F is obtained from the electron concentration n_c given by

$$n_c = \int_{-\infty}^{\infty} D(E) f(E) dE = (g_s/D_0) \sum_{n,\eta,s} f\left(E_n^{s\eta,\gamma}\right), \tag{9}$$

where $f(E_n^{s\eta,\gamma}) = (1 + \exp[\beta(E_n^{s\eta,\gamma} - E_F)])^{-1}$ is the Fermi-Dirac function with $\beta = 1/k_B T$.

The magenta solid curve in Fig. 3 shows E_F, obtained numerically from Eq. (9) for realistic values of $n_c = 1 \times 10^{17}$ m^{-2}, as a function of B; the LLs shown are the same as those in Fig. 2, i.e., spin and valley dependent, since the magnetic field lifts the spin and valley degeneracies of the $n \geqslant 1$ LLs. The additional intra-LL small jumps result from the lifting of these degeneracies; the solid and dashed curves ($n \geqslant 1$) are, respectively, for spins up and spins down in the K valley. For the K' valley the spins are reversed, e.g., for $n \geqslant 1$, the spin-up electrons in the K valley have the same energy as the spin-down ones in the K' valley. For $n \geqslant 1$ the fourfold degeneracy, due to spin and valley, of all LLs is lifted while the $n = 0$ LL in the conduction band for K valley and in the valence band for K' valley. The results for E_F in Fig. 3, with $M_z \neq 0$ and $M_v \neq 0$, correspond to the fourfold nondegenerate LLs.

Assuming a Gaussian broadening of the LLs, for zero temperature, the DOS per unit area given in Eq. (8) is written as $D(E) = (g_s g_v/(D_0 \Gamma\sqrt{2\pi})) \sum_{n,s} \exp[-(E - E_n^{s\eta,\gamma})^2/2\Gamma^2]$,

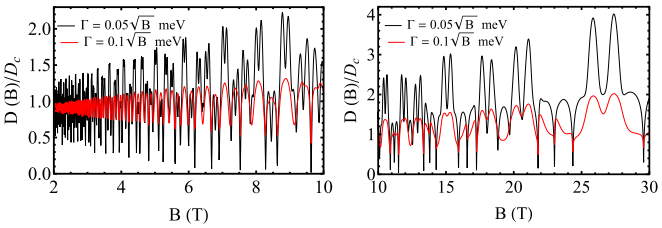

FIG. 4. Dimensionless density of states as a function of the field B for a LL width $\Gamma = 0.05\sqrt{B}$ meV (black curve) and $\Gamma = 0.1\sqrt{B}$ meV (red curve). The two panels differ only in the range of the B field (x axis).

where Γ is the width of the Gaussian distribution [26]. The DOS is shown in Fig. 4 as a function of the magnetic field, $\Gamma = 0.05\sqrt{B}$ meV (solid black), $\Gamma = 0.1\sqrt{B}$ meV (dotted red), and realistic values of $n_c = 1 \times 10^{17}$ m^{-2} [19]. We obtained the SdH oscillations as a function of magnetic field in the conduction band with equally spaced LLs. In weak magnetic fields B the level broadening effect is significant due to the small LL separation, whereas in strong fields it may become weaker due to Γ's dependence on the field as $\sqrt{B}$ and the strong LL separation.

As in the case of a 2DEG [27], the beating is due to the closeness of the frequencies of the spin-up and spin-down states that result from the splitting of the LLs due to the SOC. The beating shows up at low fields and the splitting of the oscillations becomes more pronounced at high fields. The beating persists in the conduction band for magnetic fields up to about 10 T. Above this value it is quenched and the SdH oscillations are split. This behavior is explained by the closeness of the oscillation frequencies of the SOC-split LLs. The magnetic-field-enhanced splitting in the conduction band mixes the spin-up and spin-down states of neighboring LLs into two unequally spaced energy branches. The beating appears when the subband broadening is of the order of $\hbar\omega_c$. For high magnetic fields the SOC effects weaken and the beating pattern is replaced by a splitting of the peaks, which persist due to the SOC and Zeeman energies

III. LINEAR-RESPONSE CONDUCTIVITY EXPRESSIONS

We consider a many-body system described by the Hamiltonian $H = H_0 + H_I - \mathbf{R} \cdot \mathbf{F}(t)$, where H_0 is the unperturbed part, H_I is a binary-type interaction (e.g., between electrons and impurities or phonons), and $-\mathbf{R} \cdot \mathbf{F}(t)$ is the interaction of the system with the external field $F(t)$ [28]. For conductivity problems we have $\mathbf{F}(t) = e\mathbf{E}(t)$, where $\mathbf{E}(t)$ is the electric field, e the electron charge, $\mathbf{R} = \sum_{\mathbf{r}_i}$, and $\mathbf{r}_i$ is the position operator of electron i. In the representation in which H_0 is diagonal the many-body density operator $\rho = \rho^d + \rho^{nd}$ has a diagonal part ρ^d and a nondiagonal part ρ^{nd}. For weak electric fields and weak scattering potentials, for which the first Born approximation applies, the conductivity tensor has a diagonal part $\sigma_{\mu\nu}^d$ and a nondiagonal part $\sigma_{\mu\nu}^{nd}$, $\sigma_{\mu\nu} = \sigma_{\mu\nu}^d + \sigma_{\mu\nu}^{nd}$, $\mu, \nu = x, y$.

In general we have two kinds of currents, diffusive and hopping, with $\sigma_{\mu\nu}^d = \sigma_{\mu\nu}^{\rm dif} + \sigma_{\mu\nu}^{\rm col}$, but usually only one of them is present. When a magnetic field is present we have only hopping current since the diffusive part $\sigma_{\mu\nu}^{\rm dif}$ vanishes

identically due to vanishing velocity matrix elements as is evident, for quasielastic scattering, by its form [28]

$$\sigma^{d}_{\mu\nu}(\omega) = \frac{\beta e^2}{S_0}\sum_{\zeta} f_\zeta(1-f_\zeta)\frac{v_{\nu\zeta}\, v_{\mu\zeta}\, \tau_\zeta}{1+i\omega\tau_\xi}, \tag{10}$$

where τ_ζ is the momentum relaxation time, ω the frequency, and $v_{\mu\zeta}$ the diagonal matrix elements of the velocity operator. Further, $f_\zeta = [1+\exp\beta(E_\zeta - E_F)]^{-1}$ is the Fermi-Dirac distribution function, $\beta = 1/k_BT$, T the temperature, E_F the Fermi level, and S_0 the area of the sample. In our case $v_{\mu\zeta}=0$ and the conductivity given by Eq. (10) vanishes. As for the ac hopping conductivity $\sigma^{\rm col}_{\mu\nu}$, it is given by Eq. (2.64) of Ref. [28]; in strong fields B is much smaller than the contribution $\sigma^{nd}_{\mu\nu}$ given below, and is neglected.

Regarding the contribution $\sigma^{nd}_{\mu\nu}$ one can use the identity $f_\zeta(1-f_{\zeta'})[1-\exp\beta(E_\zeta - E_{\zeta'})] = f_\zeta - f_{\zeta'}$ and cast the original form [28] in the more familiar one

$$\sigma^{nd}_{\mu\nu}(\omega) = \frac{i\hbar e^2}{S_0}\sum_{\zeta\neq\zeta'}\frac{(f_\zeta - f_{\zeta'})\, v_{\nu\zeta\zeta'}\, v_{\mu\zeta'\zeta}}{(E_\zeta - E_{\zeta'})(E_\zeta - E_{\zeta'} + \hbar\omega - i\Gamma_\zeta)}, \tag{11}$$

where the sum runs over all quantum numbers $|\zeta\rangle \equiv |n,s,k_y\rangle$ and $|\zeta'\rangle \equiv |n',s',k'_y\rangle$ with $\zeta\neq\zeta'$. The infinitesimal quantity ϵ in the original form [28] has been replaced by Γ_ζ to account for the broadening of the energy levels. Here $v_{\nu\zeta\zeta'}$ and $v_{\mu\zeta\zeta'}$ are the off-diagonal matrix elements of the velocity operator. Using Eqs. (1) and (3) for the K valley gives

$$v_{x,n,n'} = v\big[C^{s\eta,\gamma}_n D^{s\eta,\gamma'}_{n'}\delta_{n,n'-1} + D^{s\eta,\gamma}_n C^{s\eta,\gamma'}_{n'}\delta_{n-1,n'}\big]\delta_{k_y,k'_y}, \tag{12}$$

$$v_{y,n',n} = -i\eta v\big[C^{s\eta,\gamma'}_{n'} D^{s\eta,\gamma}_n\delta_{n',n-1} - D^{s\eta,\gamma'}_{n'} C^{s\eta,\gamma}_n\delta_{n'-1,n}\big]\delta_{k_y,k'_y}. \tag{13}$$

Similarly, by exchanging n with n' only in the Kronecker δ's one obtains the results for the K' valley. Since $|\zeta\rangle \equiv |n,s,k_y\rangle$, there will be one summation over k_y which, with periodic boundary conditions for k_y, gives the factor $S_0/2\pi l^2$. As usual, the matrix elements between the $n=0$ LL and the other LLs are treated separately. Using Eqs. (1) and (3), we arrive at

$$v_{x,n,n'} = v\big[D^{s\eta,\gamma'}_{n'}\delta_{0,n'-1} + D^{s\eta,\gamma}_n\delta_{0,n-1}\big], \tag{14}$$

$$v_{y,n',n} = -iv\big[D^{s\eta,\gamma'}_{n'}\delta_{0,n'-1} - D^{s\eta,\gamma}_n\delta_{0,n-1}\big]. \tag{15}$$

Similarly, by replacing D with C in Eqs. (14) and (15), we obtain the results for the K' valley. Using Eq. (12) into Eq. (11), we obtain the longitudinal component σ^{nd}_{xx} as

$$\sigma^{nd}_{xx}(\omega) = i\sigma_0\sum_{s,\eta,n,n',\gamma,\gamma'}\frac{\big(f^{s\eta,\gamma}_n - f^{s\eta,\gamma'}_{n'}\big)\big[D^{s\eta,\gamma}_n C^{s\eta,\gamma'}_{n'}\delta_{n-1,n'} + C^{s\eta,\gamma}_n D^{s\eta,\gamma'}_{n'}\delta_{n+1,n'}\big]}{\big(E^{s\eta,\gamma}_n - E^{s\eta,\gamma'}_{n'}\big)\big(E^{s\eta,\gamma}_n - E^{s\eta,\gamma'}_{n'} + \hbar\omega - i\Gamma\big)}. \tag{16}$$

The matrix elements of the velocity operators are nonzero only for $n' = n\pm 1$. Summing over n' and seting $\sigma_0 = \hbar e^2 v_F^2/(2\pi l^2)$ we arrive at

$$\sigma^{nd}_{xx}(\omega) = i\sigma_0\sum_{s,\eta,n,\gamma,\gamma'}\left[\frac{\big(f^{s\eta,\gamma}_n - f^{s\eta,\gamma'}_{n-1}\big)\, D^{s\eta,\gamma}_n C^{s\eta,\gamma'}_{n-1}}{I^{\gamma,\gamma'}_{n,n-1}\big(I^{\gamma,\gamma'}_{n,n-1} + \hbar\omega - i\Gamma\big)} + \frac{\big(f^{s\eta,\gamma}_n - f^{s\eta,\gamma'}_{n+1}\big)\, C^{s\eta,\gamma}_n D^{s\eta,\gamma'}_{n+1}}{I^{\gamma,\gamma'}_{n,n+1}\big(I^{\gamma,\gamma'}_{n,n+1} + \hbar\omega - i\Gamma\big)}\right], \tag{17}$$

where $I^{\gamma,\gamma'}_{n,n\pm1} = E^{s\eta,\gamma}_n - E^{s\eta,\gamma'}_{n\pm1}$. After making the changes $n-1\to m\to n$ in the first sum, we combine the two sums and obtain

$$\sigma^{nd}_{xx}(\omega) = i\sigma_0\sum_{s,\eta,n,\gamma,\gamma'}\left[\frac{\big(f^{s\eta,\gamma}_{n+1} - f^{s\eta,\gamma'}_{n}\big)\, D^{s\eta,\gamma}_{n+1} C^{s\eta,\gamma'}_{n}}{I^{\gamma,\gamma'}_{n+1,n}\big(I^{\gamma,\gamma'}_{n+1,n} + \hbar\omega - i\Gamma\big)} + \frac{\big(f^{s\eta,\gamma}_n - f^{s\eta,\gamma'}_{n+1}\big)\, C^{s\eta,\gamma}_n D^{s\eta,\gamma'}_{n+1}}{I^{\gamma,\gamma'}_{n,n+1}\big(I^{\gamma,\gamma'}_{n,n+1} + \hbar\omega - i\Gamma\big)}\right]. \tag{18}$$

In the limit $\Gamma\to 0$, $\omega\to 0$, and $\gamma=\gamma'$ Eq. (16) yields zero. Now, one needs to sum over all possible combinations of the matrix elements and for convenience we write $\sum_{\gamma,\gamma'} = \sum_{+,+} + \sum_{-,-} + \sum_{+,-} + \sum_{-,+}$. Here the subscript $+/-$ denotes the conduction/valence band. After performing the summation over γ,γ', we obtain the real part of σ^{nd}_{xx} as

$$\begin{aligned}\mathrm{Re}\sigma^{nd}_{xx} = -\sigma_0\sum_{\eta,s,n}\Bigg\{&\frac{\big(f^{s\eta,+}_n - f^{s\eta,+}_{n+1}\big)\Gamma\big(D^{s\eta,+}_{n+1}C^{s\eta,+}_n\big)^2}{I^{+,+}_{n,n+1}[(I^{+,+}_{n,n+1}+\hbar\omega)^2+\Gamma^2]} + \frac{\big(f^{s\eta,-}_n - f^{s\eta,-}_{n+1}\big)\Gamma\big(D^{s\eta,-}_{n+1}C^{s\eta,-}_n\big)^2}{I^{-,-}_{n,n+1}[(-I^{-,-}_{n,n+1}+\hbar\omega)^2+\Gamma^2]}\\ &+\frac{\big(f^{s\eta,-}_{n+1} - f^{s\eta,+}_n\big)\Gamma\big(D^{s\eta,-}_{n+1}C^{s\eta,+}_n\big)^2}{I^{-,+}_{n+1,n}[(I^{-,+}_{n+1,n}+\hbar\omega)^2+\Gamma^2]} + \frac{\big(f^{s\eta,-}_n - f^{s\eta,+}_{n+1}\big)\Gamma\big(D^{s\eta,+}_{n+1}C^{s\eta,-}_n\big)^2}{I^{-,+}_{n,n+1}[(I^{-,+}_{n,n+1}+\hbar\omega)^2+\Gamma^2]}\Bigg\}.\end{aligned} \tag{19}$$

Similarly, exchanging C with D in Eq. (17) gives the results for the K' valley. Following the same procedure as opted for the $n\geqslant 1$, we obtained the real part of the optical longitudinal conductivity for the $n=0$ LL as

$$\begin{aligned}\mathrm{Re}\sigma^{nd}_{xx} = -\sigma_0\sum_{\eta,s}\Bigg\{&\frac{\big[f^{s\eta,+}_0 - f^{s\eta,+}_1\big]\Gamma\big(D^{s\eta,+}_1\big)^2}{I^{+,+}_{0,1}(I^{+,+}_{0,1}+\hbar\omega)^2+\Gamma^2} + \frac{\big[f^{s\eta,-}_0 - f^{s\eta,-}_1\big]\Gamma\big(D^{s\eta,-}_1\big)^2}{I^{-,-}_{0,1}(-I^{-,-}_{0,1}+\hbar\omega)^2+\Gamma^2}\\ &+\frac{\big[f^{s\eta,-}_1 - f^{s\eta,+}_0\big]\Gamma\big(D^{s\eta,-}_1\big)^2}{I^{-,+}_{1,0}(I^{-,+}_{1,0}+\hbar\omega)^2+\Gamma^2} + \frac{\big[f^{s\eta,-}_0 - f^{s\eta,+}_1\big]\Gamma\big(D^{s\eta,+}_1\big)^2}{I^{-,+}_{0,1}(I^{-,+}_{0,1}+\hbar\omega)^2+\Gamma^2}\Bigg\}.\end{aligned} \tag{20}$$

Combining Eqs. (10), (12), and (13), carrying out the sum over n', and making the changes $n-1 \to m \to n$ in one of the sums, we obtain

$$\sigma_{xy}^{nd}(\omega) = \sigma_0 \sum_{s,\eta,n,\gamma,\gamma'} \left[\frac{\left(f_{n+1}^{s\eta,\gamma} - f_n^{s\eta,\gamma'}\right) D_{n+1}^{s\eta,\gamma} C_n^{s\eta,\gamma'}}{I_{n+1,n}^{\gamma,\gamma'}\left(I_{n+1,n}^{\gamma,\gamma'} + \hbar\omega - i\Gamma\right)} - \frac{\left(f_n^{s\eta,\gamma} - f_{n+1}^{s\eta,\gamma'}\right) C_n^{s\eta,\gamma} D_{n+1}^{s\eta,\gamma'}}{I_{n,n+1}^{\gamma,\gamma'}\left(I_{n,n+1}^{\gamma,\gamma'} + \hbar\omega - i\Gamma\right)} \right]. \tag{21}$$

Now following the same procedure as the one adopted for the nondiagonal longitudinal conductivity (17), we obtain the imaginary part of the optical Hall conductivity as

$$\begin{aligned} \mathrm{Im}\sigma_{xy}^{nd}(\omega) = -\sigma_0 \sum_{\eta,s,n} \Bigg\{ & \frac{\left(f_n^{s\eta,+} - f_{n+1}^{s\eta,+}\right)\Gamma\left(D_{n+1}^{s\eta,+} C_n^{s\eta,+}\right)^2}{I_{n,n+1}^{+,+}\left[\left(I_{n,n+1}^{+,+} + \hbar\omega\right)^2 + \Gamma^2\right]} - \frac{\left(f_n^{s\eta,-} - f_{n+1}^{s\eta,-}\right)\Gamma\left(D_{n+1}^{s\eta,-} C_n^{s\eta,-}\right)^2}{I_{n,n+1}^{-,-}\left[\left(-I_{n,n+1}^{-,-} + \hbar\omega\right)^2 + \Gamma^2\right]} \\ & - \frac{\left(f_{n+1}^{s\eta,-} - f_n^{s\eta,+}\right)\Gamma\left(D_{n+1}^{s\eta,-} C_n^{s\eta,+}\right)^2}{I_{n+1,n}^{-,+}\left[\left(I_{n+1,n}^{-,+} + \hbar\omega\right)^2 + \Gamma^2\right]} + \frac{\left(f_n^{s\eta,-} - f_{n+1}^{s\eta,+}\right)\Gamma\left(D_{n+1}^{s\eta,+} C_n^{s\eta,-}\right)^2}{I_{n,n+1}^{-,+}\left[\left(I_{n,n+1}^{-,+} + \hbar\omega\right)^2 + \Gamma^2\right]} \Bigg\}. \end{aligned} \tag{22}$$

The results for the K' valley can be obtained by exchanging C with D in Eq. (19). Following the same procedure as the one adopted for $n \geqslant 1$, we obtain the imaginary part of the optical Hall conductivity for the $n = 0$ LL as

$$\begin{aligned} \mathrm{Im}\sigma_{xy}^{nd}(\omega) = -\sigma_0 \sum_{\eta,s} \Bigg\{ & \frac{\left[f_0^{s\eta,+} - f_1^{s\eta,+}\right]\Gamma\left(D_1^{s\eta,+}\right)^2}{I_{0,1}^{+,+}\left(I_{0,1}^{+,+} + \hbar\omega\right)^2 + \Gamma^2} - \frac{\left[f_0^{s\eta,-} - f_1^{s\eta,-}\right]\Gamma\left(D_1^{s\eta,-}\right)^2}{I_{0,1}^{-,-}\left(-I_{0,1}^{-,-} + \hbar\omega\right)^2 + \Gamma^2} \\ & - \frac{\left[f_1^{s\eta,-} - f_0^{s\eta,+}\right]\Gamma\left(D_1^{s\eta,-}\right)^2}{I_{1,0}^{-,+}\left(I_{1,0}^{-,+} + \hbar\omega\right)^2 + \Gamma^2} + \frac{\left[f_0^{s\eta,-} - f_1^{s\eta,+}\right]\Gamma\left(D_1^{s\eta,+}\right)^2}{I_{0,1}^{-,+}\left(I_{0,1}^{-,+} + \hbar\omega\right)^2 + \Gamma^2} \Bigg\}. \end{aligned} \tag{23}$$

IV. NUMERICAL RESULTS AND DISCUSSION

The energies of the positive branch levels in Eq. (2) are different than those of the negative branch due to different values of the SOC energy. Because $\hbar\omega_c << \Delta$, the *intraband* and *interband* transitions in WSe_2 belong to two completely different regimes: the intraband transitions occur in the microwave-to-THz and the interband ones in the visible frequency range. We first consider the latter ones ($n' = n \pm 1$). Unlike graphenelike 2D systems, the huge band gap and strong SOC in the WSe_2 spectrum have important implications for the peaks seen in $\mathrm{Re}\sigma_{xx}^{nd}(\omega)$ and $\mathrm{Im}\sigma_{xy}^{nd}(\omega)$ as a function of the light frequency. This is shown in Fig. 5 for a temperature $T = 5$ K and a level broadening $\Gamma = 0.2\sqrt{B}$ meV. We take $B = 30$ T in order to have well-resolved LLs. The black solid curve is for E_F in the gap ($E_F = 0.0$ eV), while the red dotted curve is for $E_F = 0.892$ eV. This value falls between the $n = 3$ and $n = 4$ LLs. The optical selection rules allow n to change by only 1. In addition one needs to go from occupied to unoccupied states through the absorption of photons. For $E_F = 0$ the peaks occur at $\hbar\omega = E_{n+1}^{+} + E_n^{+}$ for integer n. The series of peaks corresponds to allowed interband transitions in the LL structure. The peak spacing is proportional to B and can be seen even at weaker fields, say, for $B \geqslant 10$ T. Similar to graphenelike 2D systems, the spectral weight of the interband peaks is continuously redistributed into the intraband peaks. This shows how the conductivity changes as E_F moves through the LLs. In contrast to graphene in which the SOC is very weak, the strong spin splitting in WSe_2 leads to beating patterns in σ_{xx} as seen in the right panel of Fig. 5. For low frequencies though, σ_{xx} doesn't show any beating pattern due to the well separated spin-up and spin-down states which do not mix at these frequencies; cf. left panel of Fig. 5.

In Fig. 6 we replot $\mathrm{Re}\sigma_{xx}^{nd}(\omega)$ with only the $n = 0$ LL taken into account. A magnetic control of the valley polarization can be clearly seen as the corresponding peaks in two different valleys appear at different frequencies. In addition to the valley-controlled transport, the spin splitting of the peaks into

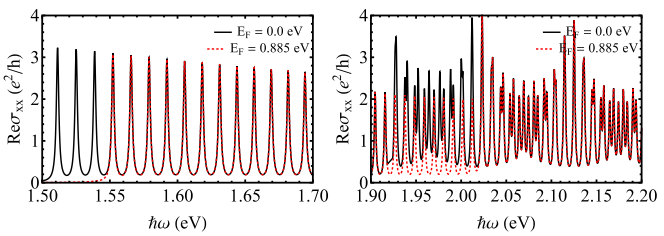

FIG. 5. Real part of the longitudinal optical conductivity as a function of the photon energy for a field $B = 30$ T. The two panels differ only in the frequency range (x axis).

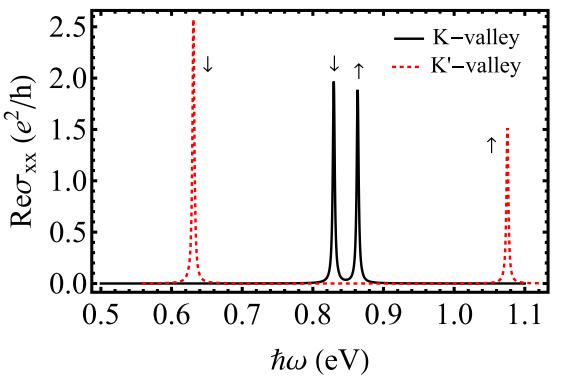

FIG. 6. As in Fig. 5 but with only the $n = 0$ LL taken into account. The spin assignment of the curves follows from Eq. (5).

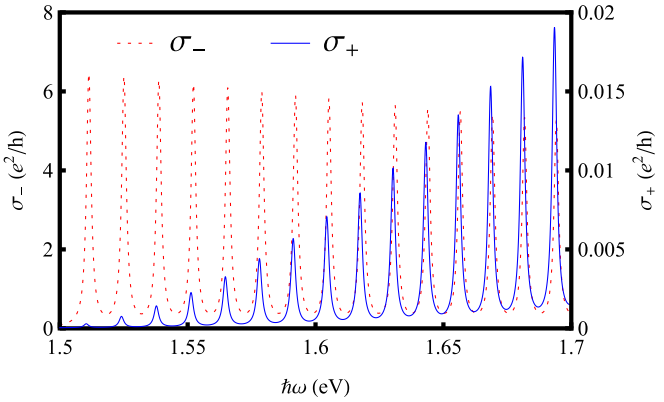

FIG. 7. Real part of the right-polarized optical conductivity $\sigma_+(\omega)$ and of the left-polarized one $\sigma_-(\omega)$ versus photon energy for $E_F = 0.0$ eV and field $B = 30$ T.

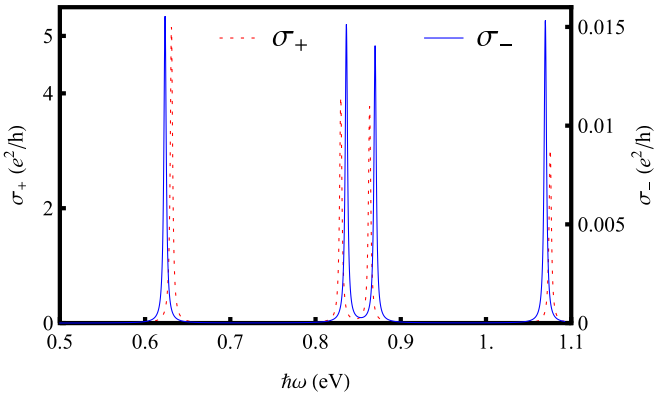

FIG. 8. As in Fig. 7 but with only the $n = 0$ LL taken into account.

two in each valley is due to the strong SOC. The spin and valley splittings can be understood with the help of Eq. (5) and the corresponding energies. This is in line with the experimental realization of the valley-controlled dynamics of particles in WSe_2 at the Dirac point due to the Zeeman term [16,17]. In the pure Dirac case the spin and valley peaks occur at the same frequency and hence cancel out perfectly in contrast to the four distinct peaks in WSe_2 shown in Fig. 6. In graphene only the first peak occurs in this conductivity component; higher-order peaks are absent due to the cancellation just described. By contrast, if we increase the value E_F so that it falls between the positive $n = 3$ and $n = 4$ LLs ($E_F = 0.885$ eV) the peaks don't cancel each other due to the asymmetric SOC splittings in the two bands. We note that the lower peaks disappear as E_F moves to higher LLs.

The peak structure just described above for $\mathrm{Re}\sigma_{xx}^{nd}(\omega)$ and $\mathrm{Im}\sigma_{xy}^{nd}(\omega)$ importantly affects their behavior for right (+) and left (−) polarized light. For real experiments that probe the (circular) polarization of resonant light, as in the case of the Kerr and Faraday effects, one evaluates the quantity $\sigma_\pm(\omega)$ given by

$$\sigma_\pm(\omega) = \mathrm{Re}\sigma_{xx}^{nd}(\omega) \mp \mathrm{Im}\sigma_{xy}^{nd}(\omega), \tag{24}$$

with the upper (lower) sign corresponding to right (left) polarization [20,21]. In Fig. 7 we show $\sigma_-(\omega)$ (solid black curve) and $\sigma_+(\omega)$ (solid red curve) as functions of the frequency, both for $E_F = 0.0$ eV in the gap, using the parameters of Fig. 5. As seen, there is a direct correspondence between these results and those of Fig. 5. The heights of the peaks in $\sigma_+(\omega)$ are much smaller than those in $\sigma_-(\omega)$. Similar to the behavior of $\mathrm{Re}\sigma_{xx}^{nd}(\omega)$ and $\mathrm{Re}\sigma_{yx}^{nd}(\omega)$, spin and valley splittings can be clearly seen in Fig. 8, in which the spin aspects of the curves are the same as in Fig. 6. We see four peaks due to the spin and valley splittings in accordance with Eq. (5) and in line with the observation of valley-controlled dynamics of particles in WSe_2 [16,17].

The difference between $\sigma_-(\omega)$ and $\sigma_+(\omega)$ is also reflected in the power absorption spectrum given by

$$P(\omega) = (E/2)[\sigma_{xx}(\omega) + \sigma_{yy}(\omega) - i\sigma_{yx}(\omega) + i\sigma_{xy}(\omega)]. \tag{25}$$

We recall that $\sigma_{\mu\nu} = \sigma_{\mu\nu}^{d} + \sigma_{\mu\nu}^{nd} = \sigma_{\mu\nu}^{nd}$ since the component $\sigma_{\mu\mu}^{d}$, $\mu = x, y$, vanishes. The component $\sigma_{yy}^{nd}(\omega)$ is given by $\sigma_{xx}^{nd}(\omega)$ and $\mathrm{Im}\sigma_{xy}^{nd}(\omega) = -\mathrm{Im}\sigma_{yx}^{nd}(\omega)$. The spectrum $P(\omega)$ is shown in Fig. 9 as a function of the photon energy for two values of E_F. Given that $\mathrm{Im}\sigma_{xy}^{nd}(\omega)$ is much smaller than $\mathrm{Re}\sigma_{xx}^{nd}(\omega)$, cf. Fig. 5, the peaks in it are essentially the same as those in the longitudinal optical conductivity. The absence of the $n \leqslant 4$ peaks for $E_F = 0.982$ eV is due to Pauli blocking and consistent with Fig. 5. Similar to the $\mathrm{Re}\sigma_{xx}^{nd}(\omega)$ and $\mathrm{Re}\sigma_{yx}^{nd}(\omega)$, spin and valley splittings can be clearly seen in Fig. 10, where we see four peaks due to these splittings in accordance with Eq. (5). We find that by changing E_F from zero to a finite value, the power absorption peaks only for one valley, as in Figs. 5–10.

Now we consider *intraband* transitions between the nth and $(n+1)$th LLs *in the conduction band*, with $E_F > 0$, in which the energy change is much smaller than E_F. This involves large values of n and is known as the semiclassical limit of the magneto-optical conductivity in which E_F is much larger than $\hbar\omega_c$. Let us assume that $E_F \approx E_n^+$ lies between the nth and $(n+1)$th LLs. The pertinent energy difference is $E_n^+ - E_{n+1}^+ = -\hbar\omega_c$. For such transitions we obtain

$$\mathrm{Re}\sigma_{xx}^{nd}(\omega) = -\sigma_0 \sum_{\eta,s,n} \frac{\left(f_n^{s\eta,+} - f_{n+1}^{s\eta,+}\right)\Gamma\left(D_{n+1}^{s\eta,+} C_n^{s\eta,+}\right)^2}{I_{n,n+1}^{+,+}[(I_{n,n+1}^{+,+} + \hbar\omega)^2 + \Gamma^2]}. \tag{26}$$

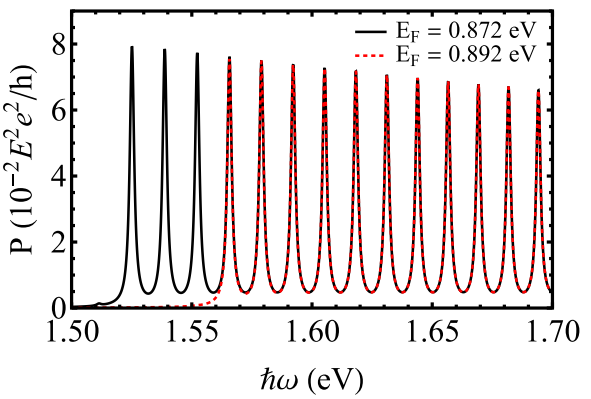

FIG. 9. Power spectrum vs photon energy for an electric field $E = 8$ V/nm, two values of E_F, and field $B = 30$ T.

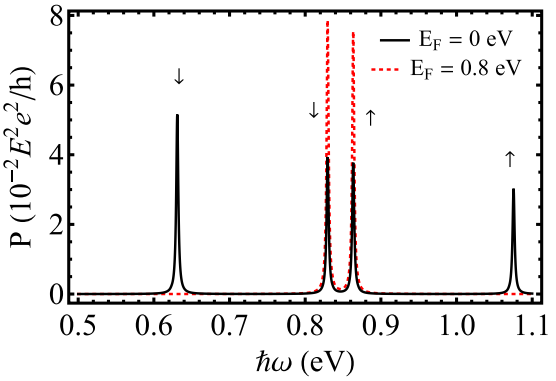

FIG. 10. Power spectrum vs photon energy for an electric field $E = 8$ V/nm, two values of E_F, field $B = 30$ T, and only the $n = 0$ LL taken into account. The spin assignment of the curves follows Eq. (5) and is identical to that of Fig. 6. The outer peaks are for the K' valley and the inner ones for the K valley.

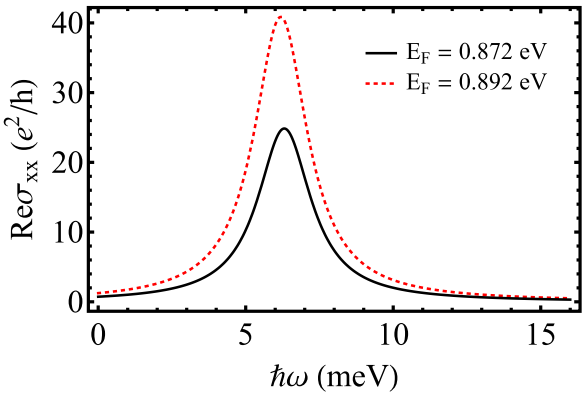

FIG. 11. Intraband limit of the real part of the longitudinal optical conductivity versus photon energy, two values of E_F, and $B = 30$ T. The energy $\hbar\omega$ is measured from the bottom of the conduction band.

The real part of $\sigma_{xx}^{nd}(\omega)$ is shown in Fig. 11. As seen, the optical spectral weight under these curves increases with E_F. These peaks lie in the range of microwave-to-THz frequencies and their height is larger than that of the interband transitions shown in Figs. 5–10. This is consistent with graphene or topological insulators and other symmetric 2D systems in which the relevant spectral weight increases with E_F, see, e.g., Fig. 7 of Ref. [29], and the optical features appear in the THz regime only [29,30].

V. SUMMARY

We studied spin- and valley-controlled magneto-optical transport properties of a WSe_2 monolayer subject to a perpendicular magnetic field. We showed periodic oscillations with frequency of the conductivities due to the absorption of photons corresponding to LL transitions induced by the pertinent selection rules. Due to the large direct band gap of WSe_2 the conductivity peaks depend linearly on B and reflect the equidistant LLs in each band. The *intraband* and *interband* optical transitions in WSe_2 belong to two completely different regimes: the intraband one is in the microwave-to-THz range and the interband one in the visible frequency range. The absorption peaks for the $n = 0$ LL appear in between these two regimes and, as Figs. 6 and 10 demonstrate, a magnetic control of the valley and spin splittings is possible. These findings expand the horizon of the electronic properties of a 2D WSe_2 system and could be useful in the design of spintronic and valleytronic optical devices.

ACKNOWLEDGMENT

This work was supported by the Canadian NSERC Grant No. OGP0121756.

[1] L. Liao, Y.-C. Lin, M. Bao, R. Cheng, J. Bai, Y. Liu, Y. Qu, K. L. Wang, Y. Huang, and X. Duan, Nature (London) **467**, 305 (2010); F. Schwierz, Nat. Nanotechnol. **5**, 487 (2010).

[2] J. Sone, T. Yamagami, Y. Aoki, K. Nakatsuji, and H. Hirayama, New J. Phys. **16**, 095004 (2014); P. D. Padova, C. Ottaviani, C. Quaresima, B. Olivieri, P. Imperatori, E. Salomon, T. Angot, L. Quagliano, C. Romano, A. Vona, M. M.- Miranda, A. Generosi1, B. Paci, and G. L. Lay, 2D Mater. **1**, 021003 (2014).

[3] M. E. Dávila, L. Xian, S. Cahangirov, A. Rubio, and G. Le. Lay, New J. Phys. **16**, 095002 (2014).

[4] A. K. Geim and I. V. Grigorieva, Nature (London) **499**, 419 (2013).

[5] B. Radisavljevic, A. Radenovic, J. Brivio, V. Giacometti, and A. Kis, Nat. Nanotechnol. **6**, 147 (2011); H. Fang, S. Chuang, T. C. Chang, K. Takei, T. Takahashi, and A. Javey, Nano Lett. **12**, 3788 (2012); H. Wang, L. Yu, Y.-H. Lee, Y. Shi, A. Hsu, M. L. Chin, L.-J. Li, M. Dubey, J. Kong, and T. Palacios, *ibid.* **12**, 4674 (2012); M. S. Fuhrer and J. Hone, Nat. Nanotechnol. **8**, 146 (2013).

[6] D. Xiao, G.-B. Liu, W. Feng, X. Xu, and W. Yao, Phys. Rev. Lett. **108**, 196802 (2012).

[7] H.-Z. Lu, W. Yao, D. Xiao, and S.-Q. Shen, Phys. Rev. Lett. **110**, 016806 (2013).

[8] X. Li, F. Zhang, and Q. Niu, Phys. Rev. Lett. **110**, 066803 (2013).

[9] A. Splendiani, L. Sun, Y. Zhang, T. Li, J. Kim, C.-Y. Chim, G. Galli, and F. Wang, Nano Lett. **10**, 1271 (2010).

[10] J. K. Ellis, M. J. Lucero, and G. E. Scuseria, Appl. Phys. Lett. **99**, 261908 (2011).

[11] H. S. Lee, S.-W. Min, Y.-G. Chang, M. K. Park, T. Nam, H. Kim, J. H. Kim, S. Ryu, and S. Im, Nano Lett. **12**, 3695 (2012).

[12] E. Cappelluti, R. Roldán, J. A. Silva-Guillén, P. Ordejón, and F. Guinea, Phys. Rev. B **88**, 075409 (2013).

[13] Q. H. Wang, K. Kalantar-Zadeh, A. Kis, J. N. Coleman, and M. S. Strano, Nat. Nanotechnol. **7**, 699 (2012).

[14] H. Liu, A. T. Neal, and P. D. Ye, ACS Nano **6**, 8563 (2012).

[15] Y. Yoon, K. Ganapathi, and S. Salahudin, Nano Lett. **11**, 3768 (2011).

[16] G. Aivazian, Z. Gong, A. M. Jones, R.-L. Chu, J. Yan, D. G. Mandrus, C. Zhang, D. Cobden, W. Yao, and X. Xu, Nat. Phys. **11**, 148 (2015).

[17] A. Srivastava, M. Sidler, A. V. Allain, D. S. Lembke, A. Kis, and A. Imamoğlu, Nat. Phys. **11**, 141 (2015).
[18] H. C. P. Movva, A. Rai, S. Kang, K. Kim, B. Fallahazad, T. Taniguchi, K. Watanabe, E. Tutuc, and S. K. Banerjee, ACS Nano **9**, 10402 (2015).
[19] A. A. Mitioglu, P. Plochocka, Á. G. del Aguila, P. C. M. Christianen, G. Deligeorgis, S. Anghel, L. Kulyuk, and D. K. Maude, Nano Lett. **15**, 4387 (2015).
[20] V. P. Gusynin, S. G. Sharapov, and J. P. Carbotte, Phys. Rev. Lett. **98**, 157402 (2007); Z. Q. Li, E. A. Henriksen, Z. Jiang, Z. Hao, M. C. Martin, P. Kim, H. L. Stormer, and D. N. Basov, Nat. Phys. **4**, 532 (2008); T. Stauber and N. M. R. Peres, J. Phys.: Condens. Matter **20**, 055002 (2008).
[21] W.-K. Tse and A. H. MacDonald, Phys. Rev. B **84**, 205327 (2011); I. Garate and M. Franz, *ibid.* **84**, 045403 (2011); D. K. Efimkin and Y. E. Lozovik, *ibid.* **87**, 245416 (2013); A. Ullah and K. Sabeeh, J. Phys.: Condens. Matter **26**, 505303 (2014); M. Lasia and L. Brey, Phys. Rev. B **90**, 075417 (2014).
[22] Z. Li and J. P. Carbotte, Phys. Rev. B **86**, 205425 (2012).
[23] L. Stille, C. J. Tabert, and E. J. Nicol, Phys. Rev. B **86**, 195405 (2012).
[24] M. Tahir, P. Vasilopoulos, and F. M. Peeters, Phys. Rev. B **92**, 045420 (2015).
[25] A. M. Jones, H. Yu, J. S. Ross, P. Klement, N. J. Ghimire, J. Yan, D. G. Mandrus, W. Yao, and X. Xu, Nat. Phys. **10**, 130 (2014).
[26] Y. Zheng and T. Ando, Phys. Rev. B **65**, 245420 (2002).
[27] X. F. Wang and P. Vasilopoulos, Phys. Rev. B **72**, 085344 (2005); **67**, 085313 (2003).
[28] M. Charbonneau, K. M. Van Vliet, and P. Vasilopoulos, J. Math. Phys. **23**, 318 (1982).
[29] P. E. C. Ashby and J. P. Carbotte, Phys. Rev. B **87**, 245131 (2013).
[30] T. Morimoto, Y. Hatsugai, and H. Aoki, Phys. Rev. Lett. **103**, 116803 (2009).